



# Lattice-matched spinel/layered double hydroxide 2D/2D heterojunction towards large-current-density overall water splitting

Jian Chen, Zheng Li, Zhenhua Li, Yangen Zhou<sup>\*</sup>, Yanqing Lai

School of Metallurgy and Environment, National Energy Metal Resources and New Materials Key Laboratory, Hunan Provincial Key Laboratory of Nonferrous Value-Added Metallurgy, Central South University, Changsha 410083, China

## ARTICLE INFO

### Keywords:

HER  
OER  
2D/2D heterojunction  
Spinel oxides  
Layered double hydroxide

## ABSTRACT

It is fascinating and challenging to construct earth-abundant first-row transition metal-based bifunctional electrocatalysts for large-scale hydrogen production via water electrolysis. Here we report a progressive conversion from spinel nanosheets to layered double hydroxide (LDH) nanosheets through the preferential dissolution of alternated layers in spinel. This process enables the formation of a lattice-matched and chemically bonded edge-to-edge spinel/LDH 2D/2D heterojunction. Significant charge redistribution at the 2D/2D heterointerface accelerates water dissociation kinetics and optimizes adsorption energy of hydrogen- and oxygen-containing intermediates. The synthesized  $\text{CoFe}_2\text{O}_4/\text{CoFe-LDH}$  2D/2D heterojunction demonstrates exceptional performance in the hydrogen evolution reaction, achieving an overpotential of 337 mV at a high current density of  $1000 \text{ mA cm}^{-2}$ , surpassing previously reported non-noble metal-based spinels and LDHs. Furthermore, its oxygen evolution reaction performance is comparable to that of typical spinel and LDH catalysts. The in-depth insights can guide rational interfacial engineering of heterogeneous catalysts for energy and environmental applications.

## 1. Introduction

Green hydrogen is considered an ideal alternative to fossil fuels due to its high calorific value (142 MJ/kg) and zero pollution [1]. Currently, electrochemical water splitting driven by green electricity is the most efficient and cost-effective method for producing green hydrogen [2,3]. Nonetheless, its industrial application at a large scale is limited by the large thermodynamic energy barriers in the cathodic hydrogen evolution reaction (HER) and the anodic oxygen evolution reaction (OER). In this regard, noble metal-based materials such as Pt,  $\text{RuO}_2$ , and  $\text{IrO}_2$  are widely recognized as state-of-the-art catalysts for HER or OER since they can significantly diminish the energy barriers during the reaction process [4,5]. Unfortunately, their widespread use in industrial water electrolysis is hindered by their high cost and scarcity [6]. Therefore, developing non-noble metal-based catalysts that meet the requirements of industrial hydrogen production has become a research priority in recent years [7,8]. Furthermore, it is desirable to develop bifunctional electrocatalysts for both OER and HER in the same electrolyte, which can simplify the manufacture of electrolyzers with reduced cost [9–11].

To date, numerous earth-abundant and non-noble metal-based compounds have been explored as bifunctional electrocatalysts for

water electrolysis, including oxides, hydroxides, chalcogenides, phosphides, nitrides, and carbides [9–15]. Among them, spinels of  $\text{M}^{\text{II}}\text{M}_2^{\text{III}}\text{O}_4$  (metallic divalent cation  $\text{M}^{\text{II}}$  and metallic trivalent cation  $\text{M}^{\text{III}}$  occupy tetrahedron sites or octahedron sites) and layered double hydroxides (LDHs) of  $\text{M}_{1-x}^{\text{II}}\text{M}_x^{\text{III}}(\text{OH})_2(\text{A}^n)_{x/n}\cdot y\text{H}_2\text{O}$  ( $\text{A}^n$  is the interlayered anions) have attracted significant attention due to their low cost, high stability, versatile redox reactions, and tunable chemical composition and microstructure [5,16,17]. While earth-abundant first-row transition metal-based spinels and LDHs are recognized as efficient OER electrocatalysts that have been widely investigated for water oxidation [18,19], their intrinsic activity in HER remains limited particularly at high current densities, exhibiting slow advancement. Because their HER activities are primarily determined by the process of water dissolution to form adsorbed hydrogen, which is a sluggish step on spinels and LDHs [15,20]. Constructing a hierarchical three-dimensional structure represents a promising approach for enhancing HER performance by facilitating exposure of numerous active sites [21–23]. Regulating electronic structure of active sites to optimize adsorption energy of HER intermediates is another effective strategy, mainly via heteroatom incorporation [13,24,25], defect engineering [26], and heterointerface formation [27]. However, the reported activities of spinels and LDHs for

<sup>\*</sup> Corresponding author.

E-mail address: [zhouyangen@csu.edu.cn](mailto:zhouyangen@csu.edu.cn) (Y. Zhou).

<https://doi.org/10.1016/j.apcatb.2024.124204>

Received 19 February 2024; Received in revised form 29 April 2024; Accepted 14 May 2024

Available online 15 May 2024

0926-3373/© 2024 Elsevier B.V. All rights are reserved, including those for text and data mining, AI training, and similar technologies.

HER still fall short of practical applications. Lattice-matched heterointerfaces are currently demonstrated to more effectively enhance HER performance than the often-reported lattice-mismatched heterointerfaces [28–30]. Moreover, 2D/2D heterojunctions have attracted extensive interest recently due to their exciting behaviors in energy conversion systems as well as electronic/optoelectronic devices. However, fabrication of lattice-matched and chemically bonded 2D/2D heterointerfaces between oxides and hydroxides as bifunctional catalysts for overall water splitting remains a great challenge.

Here, we report the construction of a lattice-matched edge-to-edge spinel/LDH 2D/2D heterojunction during progressive topological conversion from spinel nanosheets to LDH nanosheets as an excellent bifunctional catalyst for alkaline water electrolysis. Interestingly, the preferential dissolution of alternated layers in spinel during this conversion process leads the nanosheet morphology not to be damaged. The formed lattice-matched and chemically bonded 2D/2D heterointerface between spinel and LDH facilitates the adsorption behaviour of reactive intermediates and mass transfer processes. Using the topological conversion of spinel  $\text{CoFe}_2\text{O}_4$  (CFO) to  $\text{CoFe-LDH}$  as a typical example, both experimental investigations and density functional theory results confirm the charge rearrangement occurring between Co and Fe sites at the atomic heterointerface. The optimized electronic structure of active sites significantly reduces both  $\text{H}_2\text{O}$  dissociation energy and  $\text{O}_2$  desorption energy, thereby enhancing kinetics for both HER and OER in alkaline solution. Consequently, the lattice-matched edge-to-edge CFO/ $\text{CoFe-LDH}$  2D/2D heterojunction exhibits outstanding HER performance with a low overpotential of 337 mV under a large current density of  $1000 \text{ mA cm}^{-2}$ , beyond previous reports on spinels and LDHs. Additionally, it also shows excellent OER activity with a low overpotential of 350 mV at  $1000 \text{ mA cm}^{-2}$ . The lattice-matched 2D/2D heterointerface endows the bifunctional heterojunction catalyst with high activity and high stability during electrocatalytic reactions, even at high current densities [29]. A water electrolysis cell employing the developed 2D/2D heterojunction as both cathode and anode achieves a cell voltage of 1.93 V at  $1000 \text{ mA cm}^{-2}$ , superior to commercial  $\text{Pt/C}||\text{RuO}_2$ .

## 2. Experimental section

### 2.1. Chemical and materials

Iron foam (thickness of 2 mm, pore size 110 ppi, Kunshan Tengerhui Electronic Technology), cobalt nitrate hexahydrate ( $\text{Co}(\text{NO}_3)_2 \cdot 6 \text{H}_2\text{O}$ , aladdin, AR, 99 %), thioacetamide ( $\text{CH}_3\text{CSNH}_2$ , aladdin, AR, 99 %), thiourea ( $\text{CS}(\text{NH}_2)_2$ , aladdin, AR, 99 %), potassium hydroxide (aladdin, AR, 99 %), hydrochloric acid (Sinopharm Group, AR, 36 ~ 38 wt %), ruthenium oxide hydrate ( $\text{RuO}_2 \cdot x\text{H}_2\text{O}$ , aladdin, 99.9 %),  $\text{Pt/C}$  (Sigma-Aldrich, 20 wt % Pt). All the chemicals were used without further purification.

### 2.2. Synthesis

#### 2.2.1. Synthesis of CFO/ $\text{CoFe-LDH}$ on IF

$\text{CoFe}_2\text{O}_4/\text{CoFe-LDH}$  (CFO/ $\text{CoFe-LDH}$ ) on iron foam (IF) was acquired through a simple water bath reaction process. Firstly,  $\text{Co}(\text{NO}_3)_2 \cdot 6 \text{H}_2\text{O}$  (6 mmol) and thiourea (6 mmol) were dissolved in pure water (50 mL) with magnetic stirring for 30 min to obtain a homogeneous solution. Afterward, a rectangular piece of the IF (3 cm x 4 cm) was dipped into 1 M hydrochloric acid for 5 min. After that, the IF was rinsed several times with pure water to remove surface impurities. Subsequently, pre-treated IF was transferred to the beaker containing the above solution. The beaker was heated at  $80^\circ\text{C}$  for 3 h. The resulting catalyst was washed with ethanol and water three times and dried at room temperature overnight.

#### 2.2.2. Synthesis of CFO on IF

The synthesis of CFO on IF was similar to CFO/ $\text{CoFe-LDH}$ , except

that thiourea is replaced by thioacetamide in the reactants.

#### 2.2.3. Preparation of the $\text{Pt/C}$ ( $\text{RuO}_2$ ) catalyst on IF

The commercial  $\text{Pt/C}$  ( $\text{RuO}_2$ ) powders (50 mg) were firstly dispersed in 960  $\mu\text{L}$  of an 8:2 (v/v) water/ethanol mixture and 40  $\mu\text{L}$  of Nafion solution (5 wt %) to form a homogeneous ink that took continuous sonication for at least 30 min. The prepared ink was then dropped onto an IF substrate ( $1 \text{ cm} \times 1 \text{ cm}$ ) with a mass loading of  $5 \text{ mg cm}^{-2}$ . Such  $\text{Pt/C}$  ( $\text{RuO}_2$ ) powders coated IF substrate served as a working electrode.

### 2.3. Characterizations

The microstructures of the catalysts were observed by scanning electron microscopy (SEM, TESCA NMIRA3 LMU) and transmission electron microscopy (TEM Tecnai G2 F20 S-TWIN TMP). The Elemental composition of catalysts was investigated by Oxford energy-dispersive X-ray spectrometer (EDX), which is attached to TEM equipment. The crystalline structures of materials were identified by powder X-ray diffraction (XRD, Empyrean, Malvern Panalytical) using  $\text{Cu-K}\alpha$  radiation. The X-ray photoelectron spectroscopy (XPS) analysis was measured on an ESCALAB 250Xi X-ray photoelectron spectrometer using  $\text{Mg-K}\alpha$  radiation. Raman (Thermo Scientific DXR2) spectra were obtained using a DXR2 Raman Microscope with a wavelength of 532 nm.

### 2.4. Electrochemical measurements

All the electrochemical measurements were carried out in a typical three-electrode system using a Gamry Interface 1000 electrochemical workstation at room temperature. The as-prepared catalysts were used directly as the working electrode. A Pt plate and  $\text{Hg/HgO}$  (1 M KOH) served as the counter electrode and the reference electrode, respectively. Using this three-electrode system, the as-obtained catalysts were subjected to linear sweep voltammetry (LSV) at a scan rate of  $2 \text{ mV} \cdot \text{s}^{-1}$  with 100 % ohmic potential drop (iR) correction. The measured potentials were normalized to a reversible hydrogen electrode (RHE) based on the Nernst equation:

$$E(\text{RHE}) = E(\text{Hg/HgO}) + 0.0591 \times \text{pH} + 0.098$$

The Tafel slopes were calculated based on the equation:

$$\eta = b \times \log|j| + a$$

Where  $\eta$ ,  $a$ ,  $b$ , and  $j$  are denoted as the overpotential, the Tafel constant, the Tafel slope, and the current density, respectively, which were derived from LSV curves.

The ECSA of each sample can be evaluated from electrochemical double capacitance ( $C_{dl}$ ) according to the following equation:

$$\text{ECSA} = \frac{C_{dl}}{C_s}$$

Where  $C_s$  is the specific capacitance of the sample or the capacitance of an atomically smooth planar surface of the material per unit area under identical electrolyte conditions.  $C_{dl}$  in the Faradaic potential region is calculated by linear fitting. The  $C_s$  are usually found to be in the range of  $0.02 \sim 0.06 \text{ mF cm}^{-2}$ , and it is assumed as  $0.04 \text{ mF cm}^{-2}$  per  $\text{cm}^2$  in the calculations of ECSA. The Faradaic efficiency (FE) is calculated according to the following relationship:

$$\text{FE} = \frac{2F \times n_{\text{H}_2}}{Q} = \frac{2F \times n_{\text{H}_2}}{It}$$

Where  $n_{\text{H}_2}$  is the amount of hydrogen (mol),  $F$  is the Faraday constant (96500 C/mol),  $Q$  is the total amount of charges passed through the cell,  $I$  is the current, and  $t$  is the collection time.

### 3. Results and discussion

The conversion of LDHs to spinels can be easily achieved through high-temperature calcination [31,32]. The resulting spinels from LDHs nanosheets exist as small nanoparticles, which are either interconnected to form porous nanosheets or dispersed onto two-dimensional carbon materials [33,34]. Although spinel/LDH heterojunctions have been reported several times before as catalysts for water electrolysis (Table S1), all of them exhibit almost non-conformal 0D/2D or 1D/2D structures. Such non-conformal structures are highly susceptible to mismatched weakly interacting heterointerfaces, hardly fulfilling the catalytic demands at high current densities. Consequently, it is difficult for spinel/LDH heterojunction catalysts to exhibit excellent HER performance at high current densities. This study presents a low-temperature wet chemical process for progressive conversion of spinel nanosheets to LDH nanosheets and construction of a lattice-matched edge-to-edge spinel/LDH 2D/2D heterojunction. The conversion process is shown schematically in Fig. 1. The crystal structure of spinel on the (111) plane exhibits an alternating arrangement of L1 and L2 layers. The L1 layer consists of metal-oxygen octahedra sharing edges, while the L2 layer comprises metal-oxygen octahedra and tetrahedra sharing vertices. Obviously, the thermodynamic stability of the L1 layer surpasses that of the L2 layer. Consequently, it can be hypothesized that preferential dissolution of the L2 layer over the L1 layer would occur in a specific reaction environment. Interestingly, the arrangement of metal-oxygen octahedra in the L1 layer of spinel closely resembles that found in the LDH's layered framework structure (i.e. L3 layer, only with some metal-oxygen octahedra missing in the L1 layer). During the dissolution of the L2 layer, hydrolysis would take place on surface of the retained L1 layers, resulting in gradual conversion from spinel to LDH without any microstructural collapse. In this conversion process, the atomic arrangement of spinel's L1 layer is almost inherited by LDH's L3 layer, as an unchanged common layered framework structure. Additionally, dissolved metal ions from the L2 layer would deposit at the edge of the L3 layer or fill the vacancies of metal-oxygen octahedra in the L3 layer. Therefore, lattice-matched and chemically bonded edge-to-edge spinel/LDH 2D/2D heterojunction could be constructed during this topological conversion process (Fig. 1).

The synthesis of CFO/CoFe-LDH 2D/2D heterojunction via

progressive topological conversion from CFO nanosheets to CoFe-LDH nanosheets was investigated as a typical example in this study. As depicted in Fig. 2a-c, 2D CFO nanosheets were successfully and simply synthesized on iron foam by reacting acid-pretreated iron foam (Figure S1) with a solution containing  $\text{Co}^{2+}$  ions and thioacetamide at 80 °C for 3 hours. Thioacetamide acted as a structure-directing agent, gradually releasing  $\text{NH}_3$  and  $\text{S}^{2-}$  at a high temperature [35,36]. Interestingly, when thiourea was used instead of thioacetamide under the same experimental conditions, CFO/CoFe-LDH 2D/2D heterojunctions were obtained (Fig. 2d-e). The conversion from CFO nanosheets to CoFe-LDH nanosheets was completed with a longer reaction time, while maintaining the nanosheet morphology without any microstructural collapse or new nanostructure formation (Figure. S2-3). Thiourea as a structure-directing agent also released  $\text{NH}_3$  and  $\text{S}^{2-}$  at a high temperature; however, it released more  $\text{NH}_3$  compared to thioacetamide. This excess  $\text{NH}_3$  resulted in an increase in alkaline ions within the reaction solution. These alkaline ions could attack CFO, leading to preferential dissolution of the CFO's L2 layer and subsequent progressive topological conversion from CFO nanosheets to CoFe-LDH nanosheets (as shown in Figure S4). After a reaction time of 9 hr, complete conversion from CFO nanosheets to CoFe-LDH nanosheets was observed (Fig. 2f-g). Consistent with expectations, larger nanosheets were produced with increasing topological conversion reaction time (Figure S2). To enhance the intuitive understanding of the topological conversion from CFO to CoFe-LDH, we substituted iron foam (IF) with CFO and introduced it into the thiourea system for the reaction. The XRD pattern in Fig. S5a reveals that CFO is almost completely converted to LDH after 9 h transformation reaction. As anticipated, the ultra-thin 2D nanosheet structure has been successfully retained (Fig. S5b-c). It is worth noting that sulfur (S) and nitrogen (N) originating from the structure-directing agents  $\text{NH}_3$  and  $\text{S}^{2-}$ , respectively, did not remain on the surface of the produced nanosheets (Figure S6); thus, they would not influence the electrocatalytic performance of the samples. Moreover, the wettability of the electrolyte solution on the electrode surface is closely related to its electrocatalytic performance, especially at high current densities. The 2D/2D heterojunction catalyst exhibits a stronger affinity for aqueous solutions compared to CFO, benefiting from the vigorous capillary action caused by the structure composed of larger nanosheets inherited through the topological conversion (Figure S7).

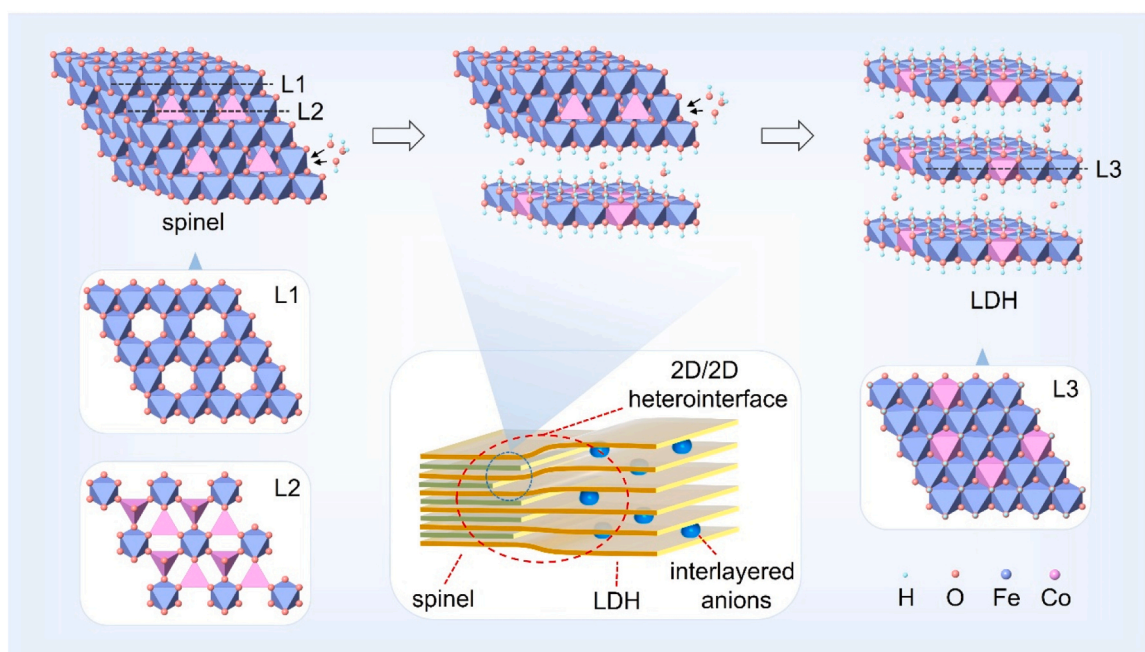
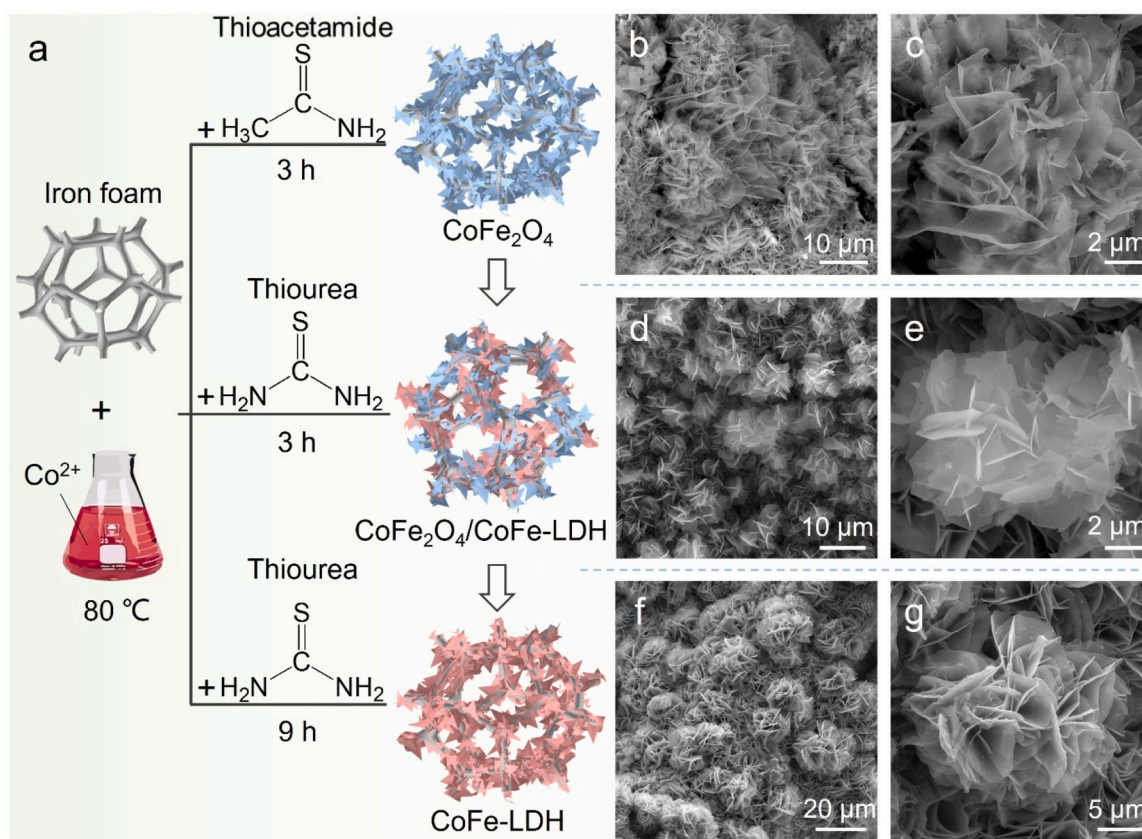


Fig. 1. Schematic illustration of topological conversion from spinel to LDH.





**Fig. 2.** (a) Schematic diagram for catalyst preparation. (b-g) SEM images of CFO nanosheets (b-c), CFO/CoFe-LDH 2D/2D heterojunctions (d-e), and CoFe-LDH nanosheets (f-g).

The formation of CFO and CFO/CoFe-LDH on iron foams was confirmed by X-ray diffraction (XRD) analysis, as shown in Fig. 3a. Additionally, the XRD results in Figure S3 provide evidence for the conversion from CFO nanosheets to CoFe-LDH nanosheets with increasing reaction time. High-resolution TEM (HRTEM) image of the as-prepared CFO/CoFe-LDH 2D/2D heterojunction is presented in Fig. 3b. The crystal structure change during the transformation from spinel CFO nanosheets to CoFe-LDH nanosheets were analyzed in Fig. 3c-d. The crystal structure of spinel on the (111) plane exhibits an alternating stacking of L1 and L2 layers (Fig. 3c). And CoFe-LDH nanosheets are constructed by selective dissolution of the L2 layer of spinel CFO nanosheets (Fig. 3d). Interestingly, due to the absence of the L2 layer, change of interplanar spacing from 0.14 nm of CFO to 0.28 nm of CoFe-LDH can be observed from the top-view crystal structures (Fig. 3c-d). This is clearly confirmed in the HRTEM image of CFO/CoFe-LDH (Fig. 3b), showing the grain boundary between CFO to CoFe-LDH. This phenomenon evidences that the topological conversion from CFO nanosheets to CoFe-LDH nanosheets leads to a well lattice-matched interface, as suggested in Fig. 1. The scanning transmission electron microscopy (STEM) image in Figure S8 confirms the 2D nanosheet morphology of CFO/CoFe-LDH, while the corresponding elemental mapping images demonstrate the uniform distribution of Co, Fe, and O elements in the sample. Compared to pure CFO, Raman spectra analysis shows that CFO/CoFe-LDH exhibits two additional peaks at 521 and  $456\text{ cm}^{-1}$  (Figure S9), which can be attributed to hydroxyl vibrations originating from CoFe-LDH [37]. This result further supports the conversion from CFO to CoFe-LDH. Electron paramagnetic resonance (EPR) spectra reveal an intense signal at  $g = 2.004$  for both CFO and CFO/CoFe-LDH, identifying the presence of oxygen vacancies (Fig. 3e) [38]. This phenomenon can be attributed to the strong reducing agent  $\text{S}^{2-}$  released during the preparation process. The strongly reductive  $\text{S}^{2-}$

could lower the oxidation state of the metal ions in CFO, leading to the creation of oxygen vacancies around the metal atoms [39,40]. Interestingly, the topological conversion of CFO nanosheets to CFO/CoFe-LDH nanosheets generates a higher abundance of oxygen vacancies. It is mainly caused by the strong interfacial interactions present at the CFO/CoFe-LDH heterointerface. When the lattice-matched and chemically bonded 2D/2D heterointerfaces are formed, an extremely strong interfacial interaction occurs, which induces charge rearrangement at the interface [28]. Correspondingly, a certain number of oxygen vacancies are created in order to balance the overall electroneutrality of the material [41]. Atomic force microscopy (AFM) image evidences the edge-to-edge CFO/CoFe-LDH 2D/2D heterojunction (Fig. 3f). After selective dissolution of the L2 layers, anions and water molecules could be inserted into the interspace between the L1 layers (i.e., L3 layers) of the CoFe-LDH nanosheets. And the formed CoFe-LDH nanosheets are thicker than the initial spinel CFO nanosheets during the transformation reaction. As a result, the nanosheet observed in the AFM image (Fig. 3f) exhibits distinct regions with two different heights, namely 8.5 nm and 6 nm, corresponding to CoFe-LDH and  $\text{CoFe}_2\text{O}_4$ , respectively. A transition region of 45–60 nm between the different height layers indicates the conversion of CFO nanosheets to CoFe-LDH nanosheets, which occurs progressively.

Quantitative XPS analysis of electrocatalysts in Figure S10 reveals that the percentage composition of Co and Fe in CFO was 29.63 % and 48.11 %, while in CFO/CoFe-LDH it was 45.74 % and 29.68 %. The atomic ratio of Co to Fe changes from 0.62:1–1.54:1 with the topological conversion from CFO to CFO/CoFe-LDH. This is because Co atoms are mainly in the tetrahedra of the spinel's L2 layer (indicated in Fig. 1), which dissolved and deposited at the edge of LDH's L3 layer during the topological conversion. As a result, Co atoms redistributed on the surface of the sample and led to an increase in the atomic ratio of Co to Fe.



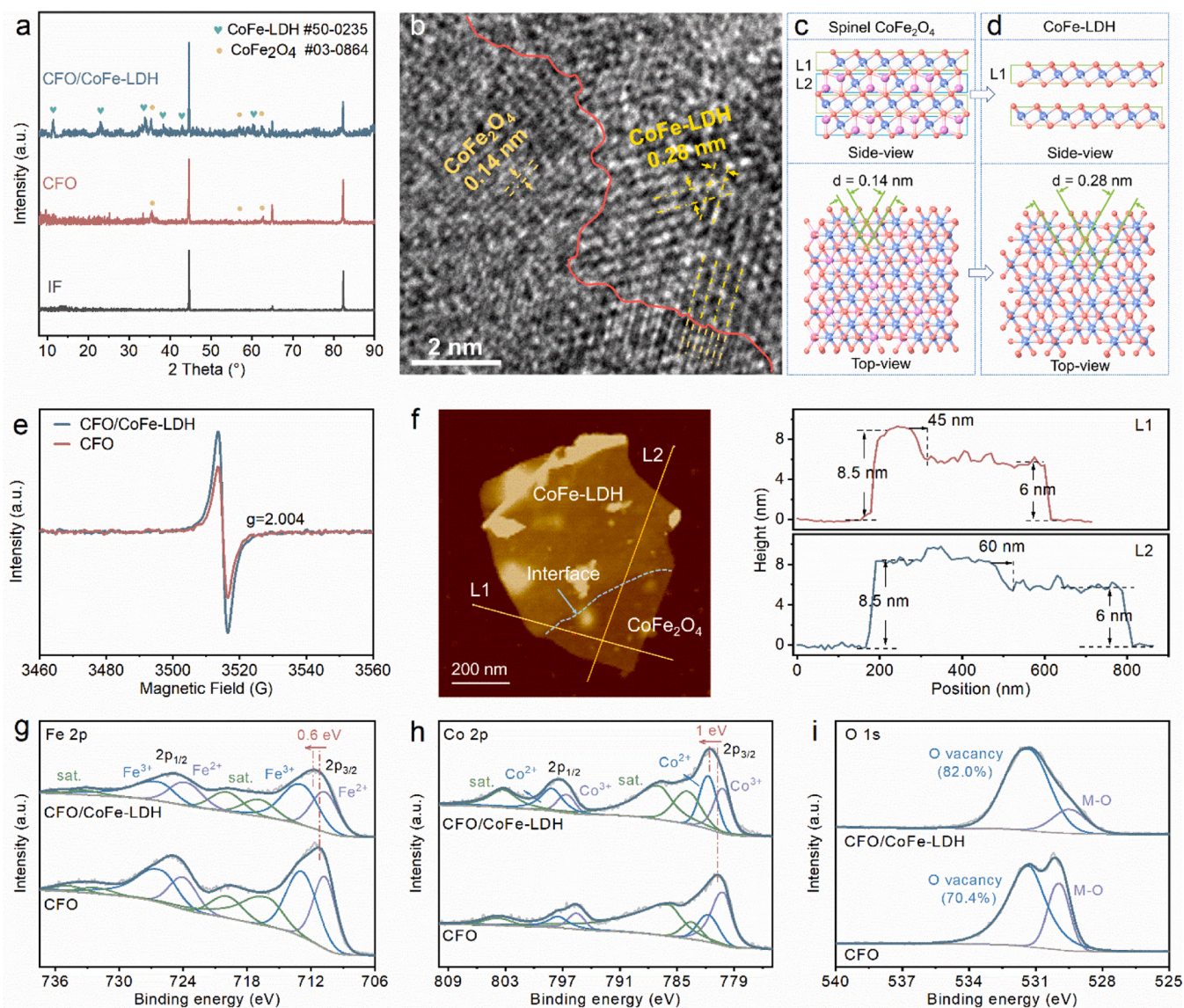


**Fig. 3.** (a) XRD patterns of CFO/CoFe-LDH, CFO, and IF. (b) HRTEM image of CFO/CoFe-LDH. (c) Crystal structure of spinel  $\text{CoFe}_2\text{O}_4$  nanosheets, the (111) facet of spinel  $\text{CoFe}_2\text{O}_4$  presents as the top-view crystal structure of the nanosheets. (d) Crystal structure of CoFe-LDH nanosheets obtained by preferential dissolution of the L2 layer of spinel  $\text{CoFe}_2\text{O}_4$ , H atoms are not shown. Red sphere: O atom, blue sphere: Co atom, purple sphere: Fe atom. (e) EPR spectra of CFO/CoFe-LDH and CFO. (f) AFM image of CFO/CoFe-LDH and corresponding height profiles of line L1 and L2; the 2D/2D heterointerface is marked by a blue dashed line. (g-i) High-resolution XPS spectra of Fe 2p, Co 2p, and O1s.

As most of CFO transform into CoFe-LDH, the Co and Fe atoms from spinel's L2 layer would be fewer than Fe atoms from iron foam to involve the growth of samples. Therefore, the atomic ratio of Co to Fe decreases to 0.74:1 after CFO completely transforming into CoFe-LDH (Figure S11). Fe 2p XPS spectra in Fig. 3g indicates the presence of both  $\text{Fe}^{2+}$  and  $\text{Fe}^{3+}$  on CFO and CFO/CoFe-LDH [42]. Obviously, a higher valence state for Fe is observed on CFO/CoFe-LDH compared to those on CFO. Similarly, both  $\text{Co}^{2+}$  and  $\text{Co}^{3+}$  appear in the two samples (Fig. 3h). In contrast, the valence of Co moves towards lower after the formation of CFO/CoFe-LDH. These results reveal that the 2D/2D heterojunction induced internal electric field effect causes the electron transfer from Fe atoms towards Co atoms within the interface region. Interestingly, this tendency of charge transfer diminishes as the degree of topological conversion deepens further until it disappears completely (Figure S12). The O 1s spectra in Fig. 3i show a peak at 529.5 eV originating from the lattice oxygen and a peak at 531.3 eV associated with the OH groups or the lattice oxygen close to oxygen vacancy [43]. It is evident that CFO/CoFe-LDH possesses a significantly higher number

of oxygen vacancies compared to CFO, which aligns with the EPR results.

The HER performance of various catalysts was evaluated in an alkaline solution (1 M KOH) using a standard three-electrode configuration (Fig. 4a). All the linear sweep voltammogram (LSV) curves were recorded at a scan rate of  $2 \text{ mV s}^{-1}$  and corrected with iR-compensation. The commercial Pt/C catalyst exhibits the smallest HER overpotential at low current densities. However, when the current density exceeds  $540 \text{ mA cm}^{-2}$ , the performance of CFO/CoFe-LDH surpasses that of the commercial Pt/C. Furthermore, Fig. 4b compares the overpotentials of the samples at the current densities of 100 and  $1000 \text{ mA cm}^{-2}$ . Under a current density of  $100 \text{ mA cm}^{-2}$ , the Pt/C catalyst displays the lowest overpotential of 153 mV, which is consistent with previous studies [44]. At a high current density of  $1000 \text{ mA cm}^{-2}$ , CFO demonstrates catalytic performance comparable to that of Pt/C due to its oxygen vacancies and unique nanosheet structure [13]. Notably, CFO/CoFe-LDH exhibits the best HER activity at  $1000 \text{ mA cm}^{-2}$  with an overpotential value of only 337 mV. However, with CFO completely transformed into LDH, the HER



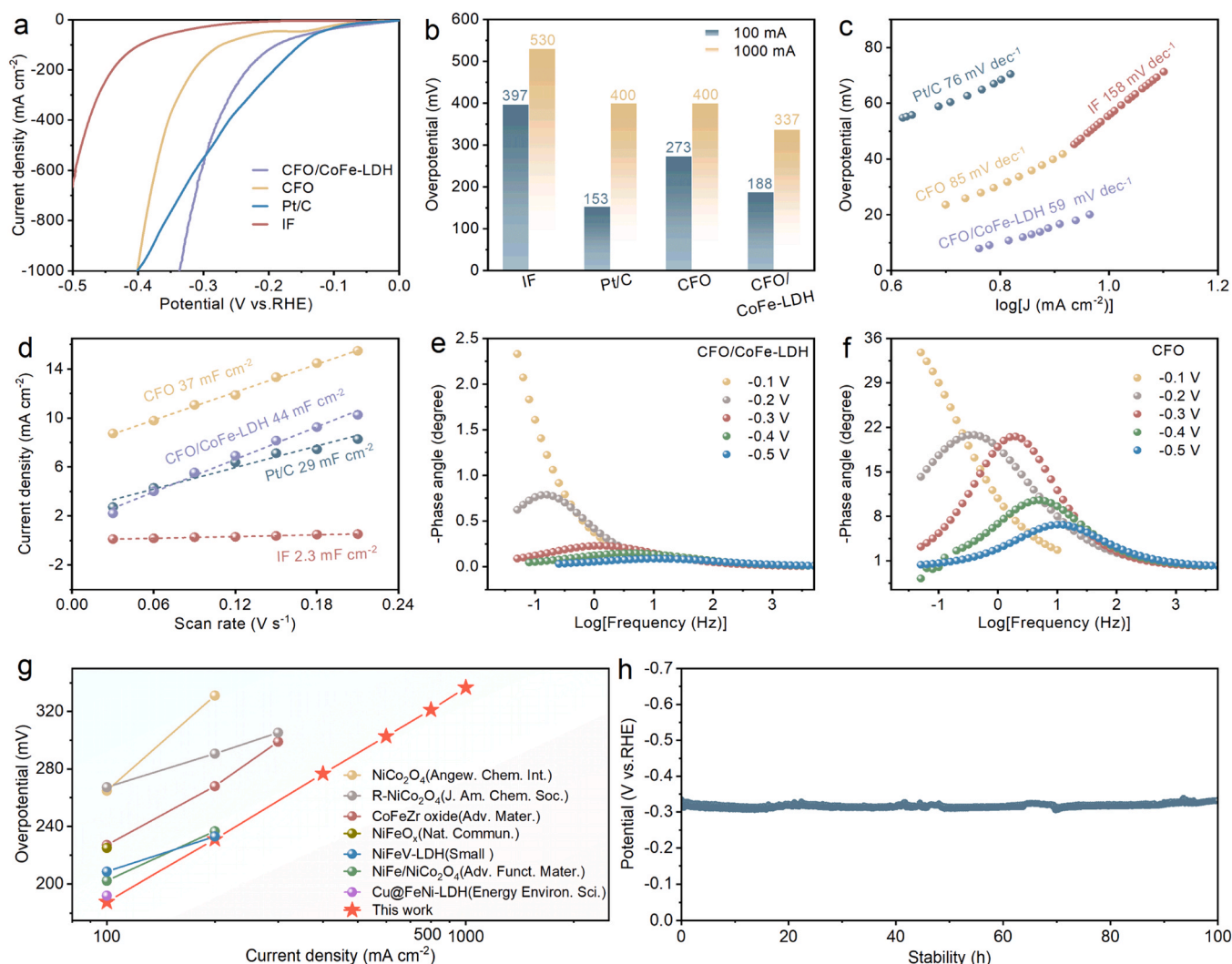


**Fig. 4.** (a) LSV curves, (b) overpotentials at the current densities of 100 and 1000 mA cm<sup>-2</sup>, (c) Tafel slopes, and (d) C<sub>dl</sub> values of CFO/CoFe-LDH, CFO, Pt/C, and IF. Bode plots of (e) CFO/CoFe-LDH and (f) CFO. (g) HER overpotentials at different current densities of reported typical non-noble metal-based spinels and LDHs (Table S2), compared with CFO/CoFe-LDH from this work. (h) Current density-time curve of CFO/CoFe-LDH for HER at 100 mA cm<sup>-2</sup>.

performance obviously decreased as expected (Figure S13). The Tafel slope value of CFO/CoFe-LDH is significantly lower than those of Pt/C and CFO, indicating its excellent HER kinetics (Fig. 4c). Electrochemical double layer capacitance (C<sub>dl</sub>) serves as a criterion for identifying exposed active sites on catalysts (Figure S14) [45]. The C<sub>dl</sub> of CFO/CoFe-LDH is 44 mF cm<sup>-2</sup>, larger than that of Pt/C (29 mF cm<sup>-2</sup>), CFO (37 mF cm<sup>-2</sup>) and IF (2.3 mF cm<sup>-2</sup>) (Fig. 4d). Correspondingly, the electrochemical surface area (ECSA) of CFO/CoFe-LDH, CFO, Pt/C, and IF are 1100, 925, 725, and 57.5 cm<sup>2</sup>, respectively (Figure S15). The turnover frequency (TOF) of the CFO/CoFe-LDH catalyst was determined to be 0.62 s<sup>-1</sup> for HER (see TOF Calculations in Supporting Information) at an overpotential of 200 mV, indicating its exceptional intrinsic activity. Overall, all these results indicate the better intrinsic HER activity of CFO/CoFe-LDH than that of spinel, LDH, and commercial Pt/C under high current densities.

Electrochemical impedance spectroscopy (EIS) was employed to investigate the charge transfer impedance of the reaction system. The Bode plots in Fig. 4e-f indicate that the equivalent circuit of electrocatalysis is characterized by a time constant, which is further confirmed by the observed only one semicircle in each Nyquist diagram (Figure S16) [46]. At potentials of 0 and -0.1 V (vs. RHE), the Nyquist plots of both CFO/CoFe-LDH and CFO are approximately a straight line, indicating that HER has not yet started. As the potential gradually

declines from -0.1 to -0.5 V (vs. RHE), the Nyquist plots of both catalysts display a semicircular curve with decreasing diameter. It indicates that the HER reaction became more and more violent, which is consistent with the corresponding Bode plots. Moreover, CFO/CoFe-LDH exhibits a lower charge transfer impedance and a much smaller phase angle than CFO at each applied potential (Fig. 4e-f). In the bode plots, the phase angle at the low-frequency region has been proved to be tightly related to water dissociation step ( $\text{H}_2\text{O} + \text{M} + \text{e}^- \rightarrow \text{M-H}_{\text{ad}} + \text{OH}^-$ ) by literature [47]. Therefore, it can be concluded that the CFO/CoFe-LDH 2D/2D heterojunction facilitates a faster water dissociation process during hydrogen evolution [48]. In general, the smaller the phase angle, the more charge is involved in the Faraday process, i.e., more charge tends to participate in redox reactions rather than forming double-layer capacitance [47,49]. The phase angle of CFO/CoFe-LDH in the Bode plots is much smaller than that of CFO at the same bias, thus indicating an ideal Faraday efficiency. This conclusion is further supported by the near 100 % Faraday efficiency achieved during overall water splitting employing CFO/CoFe-LDH catalyst at different voltages (Figure S17). Compared with the reported HER performance of non-noble metal-based spinels, LDHs, and oxide/hydroxide heterojunction, the CFO/CoFe-LDH shows superior performance especially at high current densities, due to its topological conversion induced 2D/2D heterojunction (Fig. 4g, Table S1-S2). The HER overpotential of

CFO/CoFe-LDH only increases by 4 % after running at  $100 \text{ mA cm}^{-2}$  for 100 hours, indicating its excellent electrochemical stability for HER (Fig. 4h). The phase and morphology of CFO/CoFe-LDH catalysts before and after the HER performance tests are compared in Figure S18. No clear change was observed, which indicates the excellent structure stability of the catalyst. Additionally, the high-resolution XPS spectra reveal that there is minimal alteration in the valence states of Co, Fe and O before and after HER (Figure S19). This observation evidences that the charge modulation induced by the heterojunction remains robust during the HER process.

The OER performance of CFO/CoFe-LDH 2D/2D heterojunction and CFO nanosheets are presented in Fig. 5a. Compared with CFO and commercial  $\text{RuO}_2$ , CFO/CoFe-LDH exhibits better OER activity. Specifically, CFO/CoFe-LDH only needs overpotentials of 273, 300, and 350 mV to deliver current densities of 10, 100, and  $1000 \text{ mA cm}^{-2}$  (Fig. 5b), respectively, which are superior to those of CFO (310 and 380 mV) and  $\text{RuO}_2$  (330 and 400 mV). The large overpotential observed for the substrate iron foam (IF) suggests that its contribution to the OER performance can be ignored. The current density normalized by ECSA generally provides a more accurate reflection of the intrinsic activity of the catalyst. As depicted in Figure S20, even after accounting for variations in ECSA, the CFO/CoFe-LDH catalyst continues to demonstrate superior OER performance. This result indicates that the active sites on the 2D/2D heterojunction present higher intrinsic activity than the active

sites on the initial CFO nanosheets. As displayed in Fig. 5c, CFO/CoFe-LDH demonstrates a Tafel slope of  $55 \text{ mV dec}^{-1}$ , which is lower than those of CFO ( $62 \text{ mV dec}^{-1}$ ),  $\text{RuO}_2$  ( $64 \text{ mV dec}^{-1}$ ) and IF ( $82 \text{ mV dec}^{-1}$ ). Furthermore, the CFO/CoFe-LDH catalyst exhibits a remarkable TOF value of up to  $1.03 \text{ s}^{-1}$  for OER at an overpotential of 300 mV (see TOF Calculations in Supporting Information and Figure S21). These results suggest the fast reaction kinetics over CFO/CoFe-LDH towards water oxidation. Operando EIS was conducted to investigate the effect of the heterojunction on the interfacial behavior between electrode and electrolyte. Nyquist plots are used to quantify the total impedance of CFO/CoFe-LDH and CFO during the OER process at different potentials (Figure S22), while corresponding Bode plots are shown in Fig. 5d-e. The Nyquist plots present that as applied potential increases, there is a decrease in the semicircle diameter indicating reduced charge transfer impedance. This can be attributed to intensified OER activity at higher potentials. Generally, the peak of the low-frequency phase angle in the Bode plot corresponds to surface charge conduction for water oxidation reaction [47,50]. When potential changes from 1.43 V to 1.53 V (vs. RHE), both CFO/CoFe-LDH and CFO exhibit a sharp decrease in phase angle in their respective Bode plots, indicating an onset potential for OER between these values. This result coincides with observations from Nyquist plots as well as LSV curves of CFO/CoFe-LDH and CFO. The semicircle diameter in the Nyquist plots and the phase angle in the Bode plots of CFO/CoFe-LDH exhibit smaller values compared to those of CFO

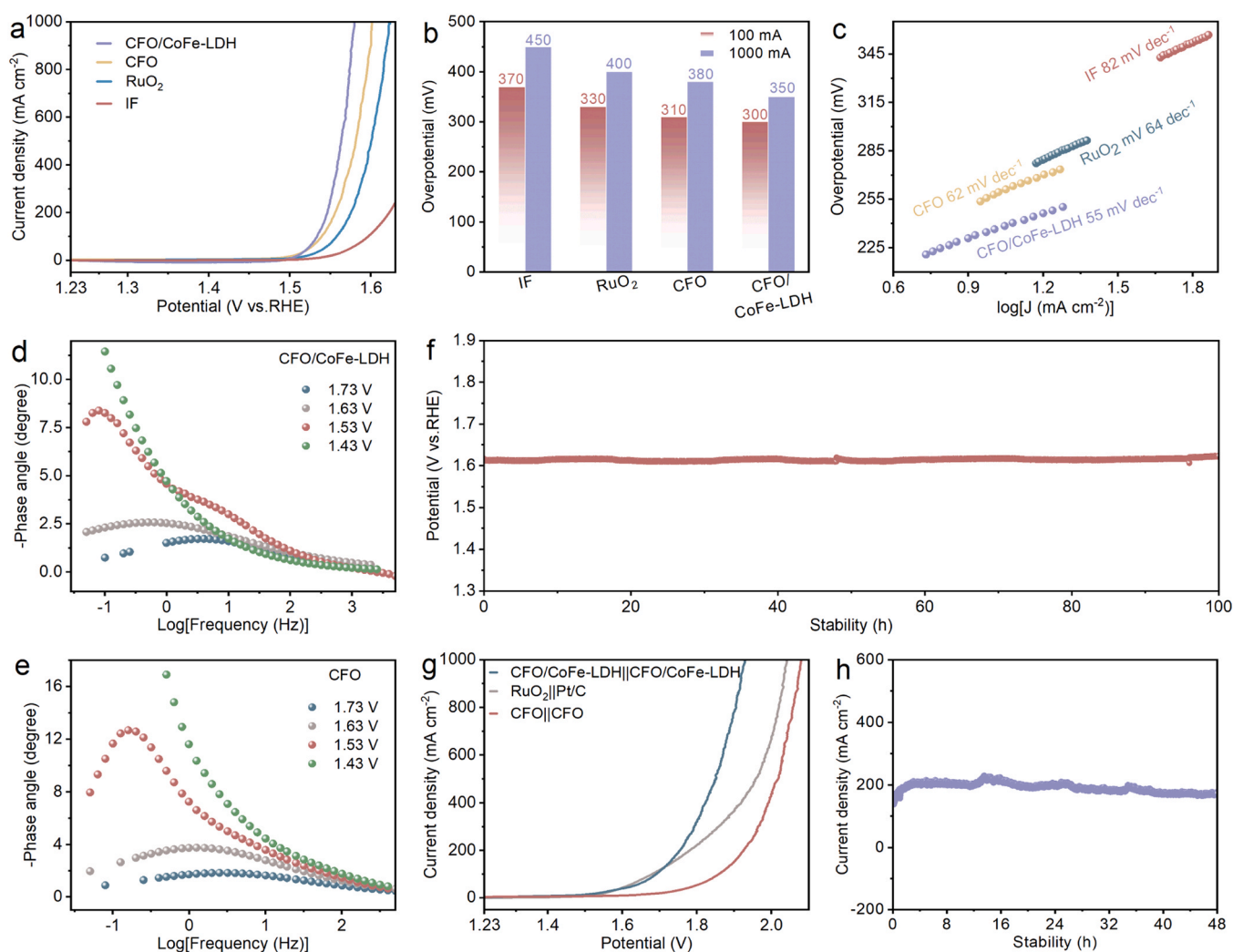


**Fig. 5.** (a) LSV curves, (b) overpotentials at  $100$  and  $1000 \text{ mA cm}^{-2}$ , (c) Tafel slopes, and (d-e) Bode plots of CFO/CoFe-LDH and CFO for OER. (f) Stability of CFO/CoFe-LDH for OER at  $100 \text{ mA cm}^{-2}$ . (g) Polarization curves of different catalysts for overall water splitting. (h) Chronopotentiometry curve of CFO/CoFe-LDH for overall water splitting at  $1.8 \text{ V}$  (with iR compensation).



under equivalent potential, indicating a lower charge transfer resistance ( $R_{ct}$ ) of CFO/CoFe-LDH for OER (Figure S23). The CFO/CoFe-LDH catalyst also exhibits comparable OER performance to that of typical spinel and LDH catalysts (Table S3), which may be attributed to its spinel/LDH 2D/2D heterojunction. The outstanding long-term stability of CFO/CoFe-LDH towards OER was verified in 1 M KOH, as evidenced by a mere 3 % increase in overpotential after operation at  $100 \text{ mA cm}^{-2}$  for 100 hours (Fig. 5f). The OER process characterized by high oxidation potentials generally induce significant alterations in the physical phase and structure of the catalyst. There is no change observed in the XRD patterns and the SEM images of CFO/CoFe-LDH catalysts before and after the OER reaction (Figure S24). These results confirm the outstanding structure stability of CFO/CoFe-LDH catalysts during OER process. Interestingly, the high-resolution XPS spectra of CFO/CoFe-LDH catalysts before and after the OER reaction reveal a significant increase in the valence state of Co, while the valence states of Fe and O remain essentially unchanged (Figure S25). This implies that the OER process on CFO/CoFe-LDH catalysts follows an adsorbate evolution mechanism (AEM) mediated by metal atom redox, with Co being identified as the primary active site for OER [51].

The above electrochemical test results suggest that the OER performance of CFO/CoFe-LDH 2D/2D heterojunction constructed by topological conversion is significantly enhanced. However, when the

topological conversion from CFO nanosheets to LDH nanosheets was completed, the resulting LDH sample exhibited inferior OER performance compared to the CFO/CoFe-LDH heterojunction (Figure S26). This can be attributed mainly to the disappearance of the internal electric field effect at the chemically bonded 2D/2D heterointerface. In addition, it is observed that the amount of thiourea added to the reaction system has an effect on the performance of the catalysts (Figure S27). In order to explore its potential for industrial applications, CFO/CoFe-LDH 2D/2D heterojunction was further employed as both cathode and anode in a water electrolysis device. CFO/CoFe-LDH achieves an overall water splitting voltage of  $1.93 \text{ V}$  at  $1000 \text{ mA cm}^{-2}$ , which is lower than that of  $\text{Pt/C}||\text{RuO}_2$  (Fig. 5g). Moreover, when used in a two-electrode system, the CFO/CoFe-LDH catalyst demonstrates stable operation at  $1.8 \text{ V}$  for more than 48 h without apparent degradation (Fig. 5h). After the overall water splitting test, no clear change was observed in the SEM images of both the HER-side and OER-side catalysts (Figure S28), which further reveals the exceptional structure stability of the bifunctional chemically bonded 2D/2D CFO/CoFe-LDH heterojunction. The Faraday efficiency of the two-electrode system was assessed with CFO/CoFe-LDH catalyst as both cathode and anode (Figure S17a). Notably, the system exhibited a near-perfect Faraday efficiency at various voltages, indicating its exceptional energy conversion efficacy (Figure S17b).

The charge rearrangement at the lattice-matched and chemically

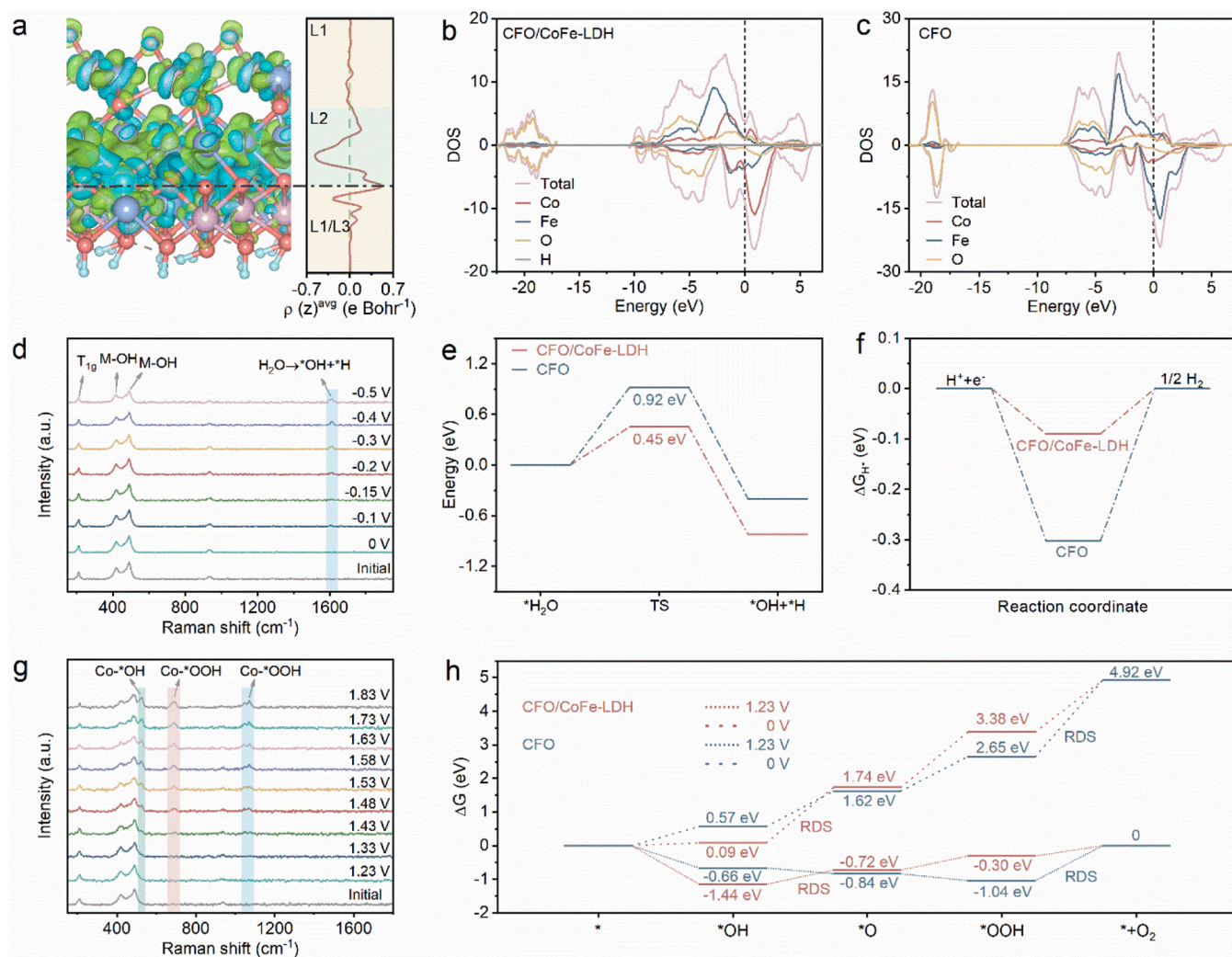


**Fig. 6.** (a) Charge density distribution at CFO/CoFe-LDH heterointerface determined by DFT calculations (green for electron depletion, cyan for electron accumulation). (b-c) Density of states curves for CFO (b) and CFO/CoFe-LDH (c). (d) In-situ Raman results of HER processes on CFO/CoFe-LDH catalyst. (e-f) DFT calculated reaction energy diagram for water dissociation (e) and HER (f) on CFO and CFO/CoFe-LDH in an alkaline environment. (g) In-situ Raman results of HER processes on CFO/CoFe-LDH catalyst. (h) DFT calculated reaction energy diagram for OER on CFO and CFO/CoFe-LDH in an alkaline environment.

bonded spinel/LDH 2D/2D heterointerface is simply depicted in Figure S29. In LDH, the interlayered anions balance the positive charges on the L3 layer induced by metallic trivalent cation  $M^{III}$  (Fig. 1). Positively charged interface layer (L1/L3) shared by spinel and LDH would induce negative charges generated on the adjacent L2 layer for charge balance. The charge redistribution at CFO/CoFe-LDH 2D/2D heterointerface was also revealed by density functional theory (DFT) calculations (Fig. 6a). As expected, the L1/L3 layer presents electron depletion. Interestingly, for the adjacent L2 layer, both sides are electron accumulation and the middle is electron depletion. This phenomenon indicates that electrons transfer from Fe atoms in the middle to Co atoms at both sides. The XPS results completely confirm this point. Moreover, the electron accumulation at the interface between L2 layer and L1/L3 layer facilitates more oxygen vacancies stabilized in the heterojunction, as revealed by EPR results. Furthermore, the electronic density of states (DOS) of CFO/CoFe-LDH and CFO were calculated (Fig. 6b-c). Both samples have a continuous energy band around the Fermi energy level, indicating that they have similar charge transport properties to metals. This phenomenon can be attributed to the doping of oxygen vacancies. Additionally, contribution of H to the total DOS is negligible, so the charges of both samples near the Fermi energy level originate from Fe, Co, and O. Importantly, Co atoms in CFO/CoFe-LDH present a significant enhancement in peak intensity of the projected density of states (PDOS) compared to that of CFO, while Fe atoms exhibit an opposite trend. These findings further support the increased charge density surrounding Co atoms in CFO/CoFe-LDH [52]. Correspondingly, this electron accumulation around Co atoms in CFO/CoFe-LDH leads to a downward shift in its d-band center (Figure S30).

The chemical properties and structural changes occurring on the CFO/CoFe-LDH surface during HER were characterized using in-situ Raman spectroscopy (Fig. 6d). The Raman peak at  $210\text{ cm}^{-1}$  originates from the  $T_{1g}$  vibration mode of  $\text{CoFe}_2\text{O}_4$ , indicating the presence of  $\text{CoFe}_2\text{O}_4$  phase [53]. The two Raman peaks located between  $400$  and  $500\text{ cm}^{-1}$  originate from the stretching vibration of M-OH related to CoFe-LDH phase, which aligns with the phenomenon depicted in Figure S9. The Raman peaks associated with CFO phase and CoFe-LDH phase remain unchanged, demonstrating the excellent structural stability of CFO/CoFe-LDH heterojunctions during HER. A new characteristic peak at  $1610\text{ cm}^{-1}$  appears as the potential decreases to  $-0.1$  (vs. RHE). This peak can be attributed to the weakening of hydrogen bonding interaction between adsorbed  $\text{H}_2\text{O}$  at the catalytic interface, indicating its preparation for subsequent charge-transfer-induced hydrolysis dissociation step [54]. Consequently, the HER on the CFO/CoFe-LDH surface initiated within the potential range of  $-0.1$  to  $-0.15\text{ V}$ , aligning consistently with the findings obtained from in-situ electrochemical impedance spectroscopy (EIS). The rate of interfacial hydrolysis dissociation gradually accelerates with decreasing the reduction potential, leading to an enhanced intensity of this peak. The HER was simulated by DFT calculations, demonstrating the significant contribution of 2D/2D heterojunction in optimizing electronic structure for accelerating HER kinetics. Co atoms on the CFO/CoFe-LDH surface were unequivocally identified as the predominant active site for HER based on rigorous theoretical calculations (Fig. 6e-f and Figures S31-S32). Previous studies have revealed that HER in alkaline media is mainly controlled by water dissociation (Figure S33) [48]. The decrease in the d-band center of Co atoms and the electron accumulation around Co atoms in CFO/CoFe-LDH allow them to have stronger adsorption of  $\text{H}_2\text{O}$  compared to Co atoms in CFO (Figure S34). As shown in Fig. 6e, the dissociation barrier of  $\text{H}_2\text{O}$  on the surface of CFO/CoFe-LDH is significantly reduced to  $0.45\text{ eV}$ , as opposed to up to  $0.92\text{ eV}$  for CFO. In addition, the charge redistribution between Co and Fe atoms in CFO/CoFe-LDH also makes the Gibbs free energy for adsorption of hydrogen intermediates ( $\Delta G_{H^*}$ ) much more preferable (Fig. 6f). These combined factors result in a significant enhancement of the alkaline HER kinetics of CFO/CoFe-LDH compared to pure CFO.

In-situ Raman techniques and DFT calculations were combined to

further explore the OER mechanism on the CFO/CoFe-LDH surface. The Raman peaks observed before  $500\text{ cm}^{-1}$  in Fig. 6g corresponding to the  $\text{CoFe}_2\text{O}_4$  and CoFe-LDH phases remains unchanged during OER. This result evidences the stable phases under high oxidation potential. When the oxidation potential reached  $1.43\text{ V}$ , the emergence of Co- $^*\text{OH}$  signal with Raman peak at  $521\text{ cm}^{-1}$  indicated the initiation of OER [55]. With increasing the oxidation potential, new Raman peaks emerged at  $683\text{ cm}^{-1}$  and  $1054\text{ cm}^{-1}$ , indicating the adsorption of  $^*\text{OOH}$  on Co sites [56,57]. This observation suggests that the OER process on the CFO/CoFe-LDH surface follows an adsorbate evolution mechanism (AEM) mediated by the redox reaction of Co sites, which is consistent with the XPS results obtained after OER tests. Additionally, the DFT results provide compelling evidence that Co atoms serve as the primary active sites in facilitating the OER process (Figure S35). Fig. 6h shows the Gibbs free energy of adsorption for intermediates ( $\Delta G$ ) along the OER pathway on the surfaces of CFO/CoFe-LDH and CFO, where the largest  $\Delta G$  is the rate-determining step (RDS) [26]. When  $U = 0\text{ V}$ , all four intermediate steps of the OER reaction occurring at the surfaces of CFO/CoFe-LDH and CFO are theoretically non-spontaneous heat absorption reactions (Figure S36). When the OER process initiates ( $U = 1.23\text{ V}$ ), the OER free energy diagram on the CFO surface suggests that the formation of  $\text{O}_2$  requires overcoming the maximum thermodynamic energy barrier ( $1.04\text{ eV}$ ), which may be caused by the difficulty of  $\text{O}_2$  desorption from the original CFO. However, the electron accumulation around the Co sites at the 2D/2D heterointerface of CFO/CoFe-LDH weakens the adsorption strength of  $\text{O}_2$ . Accordingly, the RDS changes from the formation of  $\text{O}_2$  to the deprotonation step of  $^*\text{OH}$  ( $^*\text{OH} \rightarrow ^*\text{O}$ ) with a much lower thermodynamic energy barrier of  $0.72\text{ eV}$ . Thus, at a macro level, CFO/CoFe-LDH 2D/2D heterojunction exhibits enhanced performance for OER. The number of oxygen vacancies was increased in the initial computational model for investigating the contribution of oxygen vacancies towards HER and OER. During the HER process, the added oxygen vacancies have small impact on the hydrolysis dissociation and  $\Delta G_{H^*}$  (Figure S37). This result implies that the exceptional HER performance of CFO/CoFe-LDH catalyst primarily stems from the lattice-matched and chemically bonded edge-to-edge 2D/2D heterojunctions. The generation of oxygen vacancies is necessary to maintaining charge balance at the heterointerfaces. Similar conclusions can be inferred for OER, as depicted in the Figure S38. More oxygen vacancies exhibit limited influence on the  $\Delta G$  of individual fundamental steps involved in OER and do not alter the rate-determining step (RDS) of the overall process.

#### 4. Conclusions

In summary, we reported a progressive conversion from layered spinel oxide nanosheets to corresponding LDH nanosheets, in which the common layered framework structure remains unchanged. This topological conversion results in lattice-matched and chemically bonded edge-to-edge spinel/LDH 2D/2D heterojunction. Experimental results and theoretical studies reveal unique charge redistribution at such oxide/hydroxide 2D/2D heterointerface, which accelerates both the water dissociation step in HER and the  $\text{O}_2$  desorption step in OER. Consequently, the spinel CFO/CoFe-LDH 2D/2D heterojunction demonstrates a low HER overpotential of  $337\text{ mV}$  and a low OER overpotential of  $350\text{ mV}$  at a high current density of  $1000\text{ mA cm}^{-2}$ . Notably, the HER performance of the 2D/2D heterojunction was found to be superior when contrasted with other reported non-noble metal-based spinels and LDHs to the best of our knowledge, especially at high current densities. Furthermore, the 2D/2D heterojunction can operate stably in HER and OER due to its lattice-matched and chemically bonded heterointerface. The fabrication and understanding of the lattice-matched edge-to-edge oxide/hydroxide 2D/2D heterointerface provide a favorable direction for developing excellent non-noble metal-based bifunctional catalysts for water electrolysis, which also have great potential to enhance other energy and environmental catalysis, such as fuel



cell, metal-air battery, and CO<sub>2</sub> emission reduction.

### CRediT authorship contribution statement

**Yangen Zhou:** Writing – review & editing, Visualization, Supervision, Project administration, Funding acquisition. **Yanqing Lai:** Writing – review & editing, Validation, Resources, Conceptualization. **Jian Chen:** Writing – review & editing, Writing – original draft, Visualization, Software, Methodology, Investigation, Formal analysis, Data Curation. **Zheng Li:** Writing – review & editing, Formal analysis, Investigation. **Zhenhua Li:** Writing – review & editing, Investigation, Data curation.

### Declaration of Competing Interest

The authors declare that they have no known competing financial interests or personal relationships that could have appeared to influence the work reported in this paper.

### Data Availability

Data will be made available on request.

### Acknowledgments

The authors acknowledge the financial supports from the National Natural Science Foundation of China (52374314), the Science and Technology Innovation Program of Hunan Province (2023RC3063), and Innovation Mover Program of Central South University (2023CXQD028).

### Appendix A. Supporting information

Supplementary data associated with this article can be found in the online version at [doi:10.1016/j.apcatb.2024.124204](https://doi.org/10.1016/j.apcatb.2024.124204).

### References

- [1] N. Du, C. Roy, R. Peach, M. Turnbull, S. Thiele, C. Bock, Anion-exchange membrane water electrolyzers, *Chem. Rev.* 122 (2022) 11830–11895, <https://doi.org/10.1021/acs.chemrev.1c00854>.
- [2] M. Chatenet, B.G. Pollet, D.R. Dekel, F. Dionigi, J. Deseure, P. Millet, R.D. Braatz, M.Z. Bazant, M. Eikerling, I. Staffell, P. Balcombe, Y. Shao-Horn, H. Schäfer, Water electrolysis: from textbook knowledge to the latest scientific strategies and industrial developments, *Chem. Soc. Rev.* 51 (2022) 4583–4762, <https://doi.org/10.1039/d0cs01079k>.
- [3] J. Li, C. Hou, C. Chen, W. Ma, Q. Li, L. Hu, X. Lv, J. Dang, Collaborative interface optimization strategy guided ultrafine RuCo and MXene heterostructure electrocatalysts for efficient overall water splitting, *ACS Nano* 17 (2023) 10947–10957, <https://doi.org/10.1021/acsnano.3c02956>.
- [4] L. Chong, G. Gao, J. Wen, H. Li, H. Xu, Z. Green, J.D. Sugar, A.J. Kropf, W. Xu, X.-M. Lin, H. Xu, L.-W. Wang, D.-J. Liu, La- and Mn-doped cobalt spinel oxygen evolution catalyst for proton exchange membrane electrolysis, *Science* 380 (2023) 609–616, <https://doi.org/10.1126/science.ade1499>.
- [5] Z. Li, Y.E. Zhou, M.H. Xie, H. Cheng, T. Wang, J. Chen, Y. Lu, Z.L. Tian, Y.Q. Lai, G. H. Yu, High-density cationic defects coupling with local alkaline-enriched environment for efficient and stable water oxidation, *Angew. Chem. Int. Ed.* 62 (2023) e202217815, <https://doi.org/10.1002/anie.202217815>.
- [6] B. You, Y. Sun, Innovative strategies for electrocatalytic water splitting, *Acc. Chem. Res.* 51 (2018) 1571–1580, <https://doi.org/10.1021/acs.accounts.8b00002>.
- [7] Z.Y. Yu, Y. Duan, X.Y. Feng, X. Yu, M.R. Gao, S.H. Yu, Clean and Affordable Hydrogen Fuel from Alkaline Water Splitting: Past, Recent Progress, and Future Prospects, *Adv. Mater.* 33 (2021) 2007100, <https://doi.org/10.1002/adma.202007100>.
- [8] H. Wu, C. Feng, L. Zhang, J. Zhang, D.P. Wilkinson, Non-noble metal electrocatalysts for the hydrogen evolution reaction in water electrolysis, *Electrochem. Energy Rev.* 4 (2021) 473–507, <https://doi.org/10.1007/s41918-020-00086-z>.
- [9] J. Kwon, S. Sun, S. Choi, K. Lee, S. Jo, K. Park, Y.K. Kim, H.B. Park, H.Y. Park, J. H. Jang, H. Han, U. Paik, T. Song, Tailored electronic structure of Ir in high entropy alloy for highly active and durable bifunctional electrocatalyst for water splitting under an acidic environment, *Adv. Mater.* 35 (2023) e2300091, <https://doi.org/10.1002/adma.202300091>.
- [10] T. Wu, E. Song, S. Zhang, M. Luo, C. Zhao, W. Zhao, J. Liu, F. Huang, Engineering metallic heterostructure based on Ni<sub>3</sub>N and 2M-MoS<sub>2</sub> for alkaline water electrolysis with industry-compatible current density and stability, *Adv. Mater.* 34 (2022) 2108505, <https://doi.org/10.1002/adma.202108505>.
- [11] Y. Zhang, S. Chen, Y. Zhang, R. Li, B. Zhao, T. Peng, Hydrogen-bond regulation of the microenvironment of Ni(II)-Porphyrin bifunctional electrocatalysts for efficient overall water splitting, *Adv. Mater.* 35 (2023) e2210727, <https://doi.org/10.1002/adma.202210727>.
- [12] A. Ali, F. Long, P.K. Shen, Innovative strategies for overall water splitting using nanostructured transition metal electrocatalysts, *Electrochem. Energy Rev.* 5 (2022) 1, <https://doi.org/10.1007/s41918-022-00136-8>.
- [13] L. Huang, D. Chen, G. Luo, Y.R. Lu, C. Chen, Y. Zou, C.L. Dong, Y. Li, S. Wang, Zirconium-regulation-induced bifunctionality in 3D cobalt-iron oxide nanosheets for overall water splitting, *Adv. Mater.* 31 (2019) e1901439, <https://doi.org/10.1002/adma.201901439>.
- [14] M. Jiang, H. Zhai, L. Chen, L. Mei, P. Tan, K. Yang, J. Pan, Unraveling the synergistic mechanism of bi-functional nickel-iron phosphides catalysts for overall water splitting, *Adv. Funct. Mater.* 33 (2023) 2302621, <https://doi.org/10.1002/adfm.202302621>.
- [15] G. Chen, T. Wang, J. Zhang, P. Liu, H. Sun, X. Zhuang, M. Chen, X. Feng, Accelerated hydrogen evolution kinetics on NiFe-layered double hydroxide electrocatalysts by tailoring water dissociation active sites, *Adv. Mater.* 30 (2018) 1706279, <https://doi.org/10.1002/adma.201706279>.
- [16] F. Cheng, J. Shen, B. Peng, Y. Pan, Z. Tao, J. Chen, Rapid room-temperature synthesis of nanocrystalline spinels as oxygen reduction and evolution electrocatalysts, *Nat. Chem.* 3 (2010) 79–84, <https://doi.org/10.1038/nchem.931>.
- [17] Z.-F. Huang, J. Song, Y. Du, S. Xi, S. Dou, J.M.V. Nsanzimana, C. Wang, Z.J. Xu, X. Wang, Chemical and structural origin of lattice oxygen oxidation in Co-Zn oxyhydroxide oxygen evolution electrocatalysts, *Nat. Energy* 4 (2019) 329–338, <https://doi.org/10.1038/s41560-019-0355-9>.
- [18] H. Xu, J. Yuan, G. He, H. Chen, Current and future trends for spinel-type electrocatalysts in electrocatalytic oxygen evolution reaction, *Coord. Chem. Rev.* 475 (2023) 214869, <https://doi.org/10.1016/j.ccr.2022.214869>.
- [19] L. Lv, Z. Yang, K. Chen, C. Wang, Y. Xiong, 2D layered double hydroxides for oxygen evolution reaction: from fundamental design to application, *Adv. Energy Mater.* 9 (2019) 1803358, <https://doi.org/10.1002/aenm.201803358>.
- [20] J. Zhang, T. Wang, P. Liu, Z. Liao, S. Liu, X. Zhuang, M. Chen, E. Zschech, X. Feng, Efficient hydrogen production on MoNi<sub>4</sub> electrocatalysts with fast water dissociation kinetics, *Nat. Commun.* 8 (2017) 15437, <https://doi.org/10.1038/ncomms15437>.
- [21] X. Gao, H. Zhang, Q. Li, X. Yu, Z. Hong, X. Zhang, C. Liang, Z. Lin, Hierarchical NiCo<sub>2</sub>O<sub>4</sub> hollow microcuboids as bifunctional electrocatalysts for overall water-splitting, *Angew. Chem. Int. Ed.* 55 (2016) 6290–6294, <https://doi.org/10.1002/anie.201600525>.
- [22] H. Wang, H.-W. Lee, Y. Deng, Z. Lu, P.-C. Hsu, Y. Liu, D. Lin, Y. Cui, Bifunctional non-noble metal oxide nanoparticle electrocatalysts through lithium-induced conversion for overall water splitting, *Nat. Commun.* 6 (2015) 7261, <https://doi.org/10.1038/ncomms8261>.
- [23] L. Yu, H. Zhou, J. Sun, F. Qin, F. Yu, J. Bao, Y. Yu, S. Chen, Z. Ren, Cu nanowires shelled with NiFe layered double hydroxide nanosheets as bifunctional electrocatalysts for overall water splitting, *Energy Environ. Sci.* 10 (2017) 1820–1827, <https://doi.org/10.1039/c7ee01571b>.
- [24] J. Jin, J. Yin, H. Liu, B. Huang, Y. Hu, H. Zhang, M. Sun, Y. Peng, P. Xi, C.H. Yan, Atomic Sulfur Filling Oxygen Vacancies Optimizes H Absorption and Boosts the Hydrogen Evolution Reaction in Alkaline Media, *Angew. Chem. Int. Ed.* 60 (2021) 14117–14123, <https://doi.org/10.1002/anie.202104055>.
- [25] K.N. Dinh, P. Zheng, Z. Dai, Y. Zhang, R. Dangol, Y. Zheng, B. Li, Y. Zong, Q. Yan, Ultrathin porous NiFeV ternary layer hydroxide nanosheets as a highly efficient bifunctional electrocatalyst for overall water splitting, *Small* 14 (2018) 1703257, <https://doi.org/10.1002/sml.201703257>.
- [26] S. Peng, F. Gong, L. Li, D. Yu, D. Ji, T. Zhang, Z. Hu, Z. Zhang, S. Chou, Y. Du, Necklace-like multishelled hollow spinel oxides with oxygen vacancies for efficient water electrolysis, *J. Am. Chem. Soc.* 140 (2018) 13644–13653, <https://doi.org/10.1021/jacs.8b05134>.
- [27] C. Xiao, Y. Li, X. Lu, C. Zhao, Bifunctional porous NiFe/NiCo<sub>2</sub>O<sub>4</sub>/Ni foam electrodes with triple hierarchy and double synergies for efficient whole cell water splitting, *Adv. Funct. Mater.* 26 (2016) 3515–3523, <https://doi.org/10.1002/adfm.201505302>.
- [28] Y. Zhang, P. Guo, S. Guo, X. Xin, Y. Wang, W. Huang, M. Wang, B. Yang, A. Jorge Sobrido, J.B. Ghasemi, J. Yu, X. Li, Gradient heating epitaxial growth gives well lattice-matched Mo<sub>2</sub>C-Mo<sub>2</sub>N heterointerfaces that boost both electrocatalytic hydrogen evolution and water vapor splitting, *Angew. Chem. Int. Ed.* 61 (2022) e202209703, <https://doi.org/10.1002/anie.202209703>.
- [29] Q. Xu, J. Zhang, H. Zhang, L. Zhang, L. Chen, Y. Hu, H. Jiang, C. Li, Atomic heterointerface engineering overcomes the activity limitation of electrocatalysts and promises highly-efficient alkaline water splitting, *Energy Environ. Sci.* 14 (2021) 5228–5259, <https://doi.org/10.1039/d1ee02105b>.
- [30] H. Yan, Y. Xie, A. Wu, Z. Cai, L. Wang, C. Tian, X. Zhang, H. Fu, Anion-modulated HER and OER activities of 3D Ni-V-based interstitial compound heterojunctions for high-efficiency and stable overall water splitting, *Adv. Mater.* 31 (2019) 1901174, <https://doi.org/10.1002/adma.201901174>.
- [31] H. Zhong, G. Gao, X. Wang, H. Wu, S. Shen, W. Zuo, G. Cai, G. Wei, Y. Shi, D. Fu, C. Jiang, L.W. Wang, F. Ren, Ion irradiation inducing oxygen vacancy-rich NiO/NiFe<sub>2</sub>O<sub>4</sub> heterostructure for enhanced electrocatalytic water splitting, *Small* 17 (2021) 2103501, <https://doi.org/10.1002/sml.202103501>.
- [32] S. Cho, J.W. Jang, K.J. Kong, E.S. Kim, K.H. Lee, J.S. Lee, Anion-doped mixed metal oxide nanostructures derived from layered double hydroxide as visible light



- photocatalysts, *Adv. Funct. Mater.* 23 (2012) 2348–2356, <https://doi.org/10.1002/adfm.201201883>.
- [33] Y. Li, H. Guo, J. Zhao, Y. Zhang, L. Zhao, R. Song, Te-doped NiFe<sub>2</sub>O<sub>4</sub> stabilized by amorphous carbon layers derived from one-step topological transitions of NiFe LDHs with significantly enhanced oxygen evolution reaction, *Chem. Eng. J.* 464 (2023) 142604, <https://doi.org/10.1016/j.cej.2023.142604>.
- [34] P. Zhang, L. Chen, L. Ge, P. Song, R. Xie, B. Wang, Y. Fu, S. Jia, T. Liao, Y. Xiong, A 3D rGO-supported NiFe<sub>2</sub>O<sub>4</sub> heterostructure from sacrificial polymer-assisted exfoliation of NiFe-LDH for efficient oxygen evolution reaction, *Carbon* 200 (2022) 422–429, <https://doi.org/10.1016/j.carbon.2022.08.085>.
- [35] W. Wang, Z. Xiong, W. He, W. Lu, H. Shi, Influence of thiourea modification on the NH<sub>3</sub>-SCR activity of CeO<sub>2</sub>: simultaneous tuning morphology and surface acidity, *J. Energy Inst.* 98 (2021) 322–333, <https://doi.org/10.1016/j.joei.2021.07.009>.
- [36] Y. Jin, H. Wang, J. Li, X. Yue, Y. Han, P.K. Shen, Y. Cui, Porous MoO<sub>2</sub> nanosheets as non-noble bifunctional electrocatalysts for overall water splitting, *Adv. Mater.* 28 (2016) 3785–3790, <https://doi.org/10.1002/adma.201506314>.
- [37] F. Yang, K. Slizoberg, I. Sinev, H. Antoni, A. Bahr, K. Ollegott, W. Xia, J. Masa, W. Grunert, B.R. Cuenya, W. Schuhmann, M. Muhler, Synergistic effect of cobalt and iron in layered double hydroxide catalysts for the oxygen evolution reaction, *ChemSusChem* 10 (2017) 156–165, <https://doi.org/10.1002/cssc.201601272>.
- [38] P. Zhou, G. Hai, G. Zhao, R. Li, X. Huang, Y. Lu, G. Wang, CeO<sub>2</sub> as an electron pump to boost the performance of Co<sub>4</sub>N in electrocatalytic hydrogen evolution, oxygen evolution and biomass oxidation valorization, *Appl. Catal. B Environ.* 325 (2023) 122364, <https://doi.org/10.1016/j.apcatb.2023.122364>.
- [39] L. Zhou, Y. Shao, F. Yin, J. Li, F. Kang, R. Lv, Stabilizing non-iridium active sites by non-stoichiometric oxide for acidic water oxidation at high current density, *Nat. Commun.* 14 (2023) 7644, <https://doi.org/10.1038/s41467-023-43466-x>.
- [40] X. Zhao, J. Wang, L. Lian, G. Zhang, P. An, K. Zeng, H. He, T. Yuan, J. Huang, L. Wang, Y.-N. Liu, Oxygen vacancy-reinforced water-assisted proton hopping for enhanced catalytic hydrogenation, *ACS Catal.* 13 (2023) 2326–2334, <https://doi.org/10.1021/acscatal.2c05376>.
- [41] J. Sun, H. Xue, N. Guo, T. Song, Y.R. Hao, J. Sun, J. Zhang, Q. Wang, Synergetic metal defect and surface chemical reconstruction into NiCo<sub>2</sub>S<sub>4</sub>/ZnS heterojunction to achieve outstanding oxygen evolution performance, *Angew. Chem. Int. Ed.* 60 (2021) 19435–19441, <https://doi.org/10.1002/anie.202107731>.
- [42] R. Liu, Y. Wang, D. Liu, Y. Zou, S. Wang, Water-plasma-enabled exfoliation of ultrathin layered double hydroxide nanosheets with multivacancies for water oxidation, *Adv. Mater.* 29 (2017) 1701546, <https://doi.org/10.1002/adma.201701546>.
- [43] J. Chen, C. Chen, M. Qin, B. Li, B. Lin, Q. Mao, H. Yang, B. Liu, Y. Wang, Reversible hydrogen spillover in Ru-WO<sub>3-x</sub> enhances hydrogen evolution activity in neutral pH water splitting, *Nat. Commun.* 13 (2022) 5382, <https://doi.org/10.1038/s41467-022-33007-3>.
- [44] T.L.L. Doan, D.C. Nguyen, S. Prabhakaran, D.H. Kim, D.T. Tran, N.H. Kim, J.H. Lee, single-atom Co-decorated MoS<sub>2</sub> nanosheets assembled on metal nitride nanorod arrays as an efficient bifunctional electrocatalyst for pH-universal water splitting, *Adv. Funct. Mater.* 31 (2021) 2100233, <https://doi.org/10.1002/adfm.202100233>.
- [45] C. Yang, R. Zhao, H. Xiang, J. Wu, W. Zhong, W. Li, Q. Zhang, N. Yang, X. Li, Ni-activated transition metal carbides for efficient hydrogen evolution in acidic and alkaline solutions, *Adv. Energy Mater.* 10 (2020) 2002260, <https://doi.org/10.1002/aenm.202002260>.
- [46] D. Merki, H. Vrubel, L. Rovelli, S. Fierro, X. Hu, Fe, Co, and Ni ions promote the catalytic activity of amorphous molybdenum sulfide films for hydrogen evolution, *Chem. Sci.* 3 (2012) 2515, <https://doi.org/10.1039/c2sc20539d>.
- [47] W. Chen, B. Wu, Y. Wang, W. Zhou, Y. Li, T. Liu, C. Xie, L. Xu, S. Du, M. Song, D. Wang, Y. Liu, Y. Li, J. Liu, Y. Zou, R. Chen, C. Chen, J. Zheng, Y. Li, J. Chen, S. Wang, Deciphering the alternating synergy between interlayer Pt single-atom and NiFe layered double hydroxide for overall water splitting, *Energy Environ. Sci.* 14 (2021) 6428–6440, <https://doi.org/10.1039/d1ee01395e>.
- [48] J. Hu, C. Zhang, L. Jiang, H. Lin, Y. An, D. Zhou, M.K. Leung, S. Yang, Nanohybridization of MoS<sub>2</sub> with layered double hydroxides efficiently synergizes the hydrogen evolution in alkaline media, *Joule* 1 (2017) 383–393, <https://doi.org/10.1016/j.joule.2017.07.011>.
- [49] D. Zhou, S. Wang, Y. Jia, X. Xiong, H. Yang, S. Liu, J. Tang, J. Zhang, D. Liu, L. Zheng, Y. Kuang, X. Sun, B. Liu, NiFe hydroxide lattice tensile strain: enhancement of adsorption of oxygenated intermediates for efficient water oxidation catalysis, *Angew. Chem. Int. Ed.* 58 (2018) 736–740, <https://doi.org/10.1002/anie.201809689>.
- [50] P. Zhai, C. Wang, Y. Zhao, Y. Zhang, J. Gao, L. Sun, J. Hou, Regulating electronic states of nitride/hydroxide to accelerate kinetics for oxygen evolution at large current density, *Nat. Commun.* 14 (2023) 1873, <https://doi.org/10.1038/s41467-023-37091-x>.
- [51] X. Wang, H. Zhong, S. Xi, W.S.V. Lee, J. Xue, Understanding of oxygen redox in the oxygen evolution reaction, *Adv. Mater.* 34 (2022) 2107956, <https://doi.org/10.1002/adma.202107956>.
- [52] L. An, H. Zhang, J. Zhu, S. Xi, B. Huang, M. Sun, Y. Peng, P. Xi, C.H. Yan, Balancing activity and stability in spinel cobalt oxides through geometrical sites occupation towards efficient electrocatalytic oxygen evolution, *Angew. Chem. Int. Ed.* 62 (2023) e202214600, <https://doi.org/10.1002/anie.202214600>.
- [53] P. Chandramohan, M.P. Srinivasan, S. Velmurugan, S.V. Narasimhan, Cation distribution and particle size effect on Raman spectrum of CoFe<sub>2</sub>O<sub>4</sub>, *J. Solid State Chem.* 184 (2011) 89, <https://doi.org/10.1016/j.jssc.2010.10.019>.
- [54] Y.-H. Wang, S. Zheng, W.-M. Yang, R.-Y. Zhou, Q.-F. He, P. Radjenovic, J.-C. Dong, S. Li, J. Zheng, Z.-L. Yang, G. Attard, F. Pan, Z.-Q. Tian, J.-F. Li, In situ Raman spectroscopy reveals the structure and dissociation of interfacial water, *Nature* 600 (2021) 81, <https://doi.org/10.1038/s41586-021-04068-z>.
- [55] H. Jia, N. Yao, C. Yu, H. Cong, W. Luo, Unveiling the electrolyte cations dependent kinetics on CoOOH-catalyzed oxygen evolution reaction, *Angew. Chem. Int. Ed.* 62 (2023) e202313886, <https://doi.org/10.1002/anie.202313886>.
- [56] Y.-H. Wang, J.-B. Le, W.-Q. Li, J. Wei, P.M. Radjenovic, H. Zhang, X.-S. Zhou, J. Cheng, Z.-Q. Tian, J.-F. Li, InSitu Spectroscopic Insight Into the Origin of the Enhanced Performance of Bimetallic Nanocatalysts Towards the Oxygen Reduction Reaction (ORR), *Angew. Chem. Int. Ed.* 58 (2019) 16062–16066, <https://doi.org/10.1002/anie.201908907>.
- [57] C. Qiao, Z. Usman, J. Wei, L. Gan, J. Hou, Y. Hao, Y. Zhu, J. Zhang, C. Cao, Efficient O-O coupling at catalytic interface to assist kinetics optimization on concerted and sequential proton-electron transfer for water oxidation, *ACS Nano* 17 (2023) 12278–12289, <https://doi.org/10.1021/acsnano.3c00893>.